



The First Habitable-zone Earth-sized Planet from TESS. II. Spitzer Confirms TOI-700 d

Joseph E. Rodriguez¹, Andrew Vanderburg^{2,28}, Sebastian Zieba³, Laura Kreidberg¹, Caroline V. Morley², Jason D. Eastman¹, Stephen R. Kane⁴, Alton Spencer⁵, Samuel N. Quinn¹, Ryan Cloutier¹, Chelsea X. Huang^{6,29}, Karen A. Collins¹, Andrew W. Mann⁷, Emily Gilbert^{8,9,10,11}, Joshua E. Schlieder^{10,11}, Elisa V. Quintana^{10,11}, Thomas Barclay^{10,11,12}, Gabrielle Suissa^{10,11,13}, Ravi kumar Kopparapu^{10,11,14}, Courtney D. Dressing¹⁵, George R. Ricker⁶, Roland K. Vanderspek⁶, David W. Latham¹, Sara Seager^{6,16,17}, Joshua N. Winn¹⁸, Jon M. Jenkins¹⁹, Zachory Berta-Thompson²⁰, Patricia T. Boyd^{10,11}, David Charbonneau¹, Douglas A. Caldwell^{19,21}, Eugene Chiang¹⁵, Jessie L. Christiansen²², David R. Ciardi²², Knicole D. Colón^{10,11}, John Doty²³, Tianjun Gan²⁴, Natalia Guerrero⁶, Maximilian N. Günther^{6,29}, Eve J. Lee²⁵, Alan M. Levine⁶, Eric Lopez^{10,11}, Philip S. Muirhead²⁶, Elisabeth Newton²⁷, Mark E. Rose¹⁹, Joseph D. Twicken^{19,21}, and Jesus Noel Villaseñor⁶

¹ Center for Astrophysics|Harvard & Smithsonian, 60 Garden Street, Cambridge, MA 02138, USA; joseph.rodriguez@cfa.harvard.edu

² Department of Astronomy, The University of Texas at Austin, Austin, TX 78712, USA

³ Universität Innsbruck, Institut für Astro- und Teilchenphysik, Technikerstraße 25, A-6020 Innsbruck, Austria

⁴ Department of Earth and Planetary Sciences, University of California, Riverside, CA 92521, USA

⁵ Danbury High School, Danbury, CT 06811, USA

⁶ Department of Physics and Kavli Institute for Astrophysics and Space Research, Massachusetts Institute of Technology, Cambridge, MA 02139, USA

⁷ Department of Physics and Astronomy, University of North Carolina at Chapel Hill, Chapel Hill, NC 27599, USA

⁸ Department of Astronomy and Astrophysics, University of Chicago, Chicago, IL 60637, USA

⁹ The Adler Planetarium, 1300 South Lakeshore Drive, Chicago, IL 60605, USA

¹⁰ Exoplanets and Stellar Astrophysics Laboratory, Code 667, NASA Goddard Space Flight Center, Greenbelt, MD 20771, USA

¹¹ GSFC Sellers Exoplanet Environments Collaboration, NASA Goddard Space Flight Center, Greenbelt, MD 20771, USA

¹² University of Maryland, Baltimore County, 1000 Hilltop Circle, Baltimore, MD 21250, USA

¹³ Goddard Earth Sciences Technology and Research (GESTAR), Universities Space Research Association, Columbia, MD, USA

¹⁴ NASA NExSS Virtual Planetary Laboratory, Box 951580, Seattle, WA 98195, USA

¹⁵ Department of Astronomy, University of California Berkeley, Berkeley, CA 94720-3411, USA

¹⁶ Department of Earth, Atmospheric and Planetary Sciences, Massachusetts Institute of Technology, Cambridge, MA 02139, USA

¹⁷ Department of Aeronautics and Astronautics, Massachusetts Institute of Technology, 77 Massachusetts Avenue, Cambridge, MA 02139, USA

¹⁸ Department of Astrophysical Sciences, Princeton University, 4 Ivy Lane, Princeton, NJ 08544, USA

¹⁹ NASA Ames Research Center, Moffett Field, CA 94035, USA

²⁰ Department of Astrophysical and Planetary Sciences, University of Colorado, Boulder, CO 80309, USA

²¹ SETI Institute, Mountain View, CA 94043, USA

²² Caltech/IPAC, 1200 E. California Boulevard, Pasadena, CA 91125, USA

²³ Noqsi Aerospace, Ltd., 15 Blanchard Avenue, Billerica, MA 01821, USA

²⁴ Department of Astronomy and Tsinghua Centre for Astrophysics, Tsinghua University, Beijing 100084, People's Republic of China

²⁵ Department of Physics and McGill Space Institute, McGill University, 3550 Rue University, Montreal, QC, H3A 2T8, Canada

²⁶ Department of Astronomy & Institute for Astrophysical Research, Boston University, 725 Commonwealth Avenue, Boston, MA 02215, USA

²⁷ Department of Physics and Astronomy, Dartmouth College, Hanover, NH, USA

Received 2019 December 20; revised 2020 May 22; accepted 2020 May 26; published 2020 August 14

Abstract

We present Spitzer 4.5 μm observations of the transit of TOI-700 d, a habitable-zone Earth-sized planet in a multiplanet system transiting a nearby M-dwarf star (TIC 150428135, 2MASS J06282325–6534456). TOI-700 d has a radius of $1.144^{+0.062}_{-0.061} R_{\oplus}$ and orbits within its host star's conservative habitable zone with a period of 37.42 days ($T_{\text{eq}} \sim 269$ K). TOI-700 also hosts two small inner planets ($R_b = 1.037^{+0.065}_{-0.064} R_{\oplus}$ and $R_c = 2.65^{+0.16}_{-0.15} R_{\oplus}$) with periods of 9.98 and 16.05 days, respectively. Our Spitzer observations confirm the Transiting Exoplanet Survey Satellite (TESS) detection of TOI-700 d and remove any remaining doubt that it is a genuine planet. We analyze the Spitzer light curve combined with the 11 sectors of TESS observations and a transit of TOI-700 c from the LCOGT network to determine the full system parameters. Although studying the atmosphere of TOI-700 d is not likely feasible with upcoming facilities, it may be possible to measure the mass of TOI-700 d using state-of-the-art radial velocity (RV) instruments (expected RV semiamplitude of ~ 70 cm s⁻¹).

Unified Astronomy Thesaurus concepts: Exoplanets (498); Habitable planets (695); Habitable zone (696); Low mass stars (2050); Antarctic observatories (47); Exoplanet astronomy (486); Exoplanet detection methods (489); Exoplanet systems (484)

Supporting material: data behind figures

1. Introduction

Humans have wondered for centuries whether life exists elsewhere in the universe. Thanks to new technologies and

rapid advancements in the study of exoplanets in the past few decades, we are making progress toward answering this question scientifically. So far, thousands of small exoplanets are known, most of which were discovered by the Kepler mission (Borucki et al. 2010), and astronomers have taken the first steps toward probing their compositions (e.g., Dressing et al. 2015;

²⁸ NASA Sagan Fellow.

²⁹ Juan Carlos Torres Fellow.

Rogers 2015) and atmospheres (e.g., Kreidberg et al. 2014). Now, more-sensitive instruments (e.g., Szentgyorgyi et al. 2016) and telescopes (e.g., Gardner et al. 2006; Gaudi et al. 2018; Roberge & Moustakas 2018) are planned with the eventual goal of detecting biosignatures, in an Earth-like planetary atmosphere.

Though the possibility of detecting biosignatures in the future seems real, the prospects remain uncertain. Statistical results from Kepler have shown that small, habitable-zone planets are common around low-mass host stars (Dressing & Charbonneau 2015), but it is not clear how much these planets resemble Earth. Kepler discovered potentially rocky habitable-zone planets around M-dwarf stars (Quintana et al. 2014), but they orbit stars too faint for precise radial velocity (RV) measurements, so we do not know if they are rocky like Earth or if they are shrouded by thick atmospheres, inhospitable to life as we know it. Our best constraints on which planets are rocky and which have thick envelopes come from observations of highly irradiated, hot planets (Rogers 2015; Wolfgang & Lopez 2015). So far, very few temperate planets that are similar to the size of Earth orbit host stars bright enough to carry out precise mass measurements through radial velocities.

Learning more about small, temperate planets requires finding such planets around brighter stars. In 2018 April, NASA’s Transiting Exoplanet Survey Satellite (TESS) mission launched with precisely this goal. So far, TESS has discovered over 1000 exoplanet candidates orbiting some of the brightest and closest stars to the Sun (Ricker et al. 2015; N. Guerrero et al. 2020, in preparation). Most of these planets orbit close to their stars and have high equilibrium temperatures, which allow us to study planets in highly irradiated environments and probe atmospheric loss (e.g., Kreidberg et al. 2019; Vanderspek et al. 2019). TESS is also expected to discover a small number of planets in temperate orbits around low-mass M-dwarf stars, possibly including rocky planets orbiting in their stars’ circumstellar habitable zones (Sullivan et al. 2015; Kaltenegger et al. 2019). Though TESS has detected slightly larger planets in temperate orbits (e.g., Günther et al. 2019) and terrestrial planets in hot orbits (e.g., Winters et al. 2019), so far no potentially rocky, habitable-zone planets have been reported.

In this paper, we confirm the first Earth-sized planet orbiting in its host star’s habitable zone discovered by TESS. The planet, TOI-700 d, is only $22\% \pm 7\%$ larger than Earth, orbits an M-dwarf star ($0.415 M_{\odot}$, TIC 150428135) located 31 pc from the Sun, and is a promising target for future observations to measure its mass. Unfortunately, atmospheric characterization will likely not be feasible with the James Webb Space Telescope (JWST; Beichman et al. 2014). In a companion to this paper, Gilbert et al. (2020) characterize the TOI-700 system and statistically validate TOI-700 d and two other planets in the system. TOI-700 d will likely be an attractive target for future observations, so independent confirmation of the planet’s existence is valuable before investing large amounts of telescope resources. Here, we present Spitzer Space Telescope observations that confirm TOI-700 d is a transiting planet and help to refine our knowledge of its parameters. Our paper is organized as follows: in Section 2 we discuss the TESS and Spitzer observations and reduction methods. We present our global analysis using EXOFASTv2 (Eastman et al. 2013, 2019) in Section 3. We place TOI-700 d in the context of presently known planets and examine future

prospects for characterizing the planet’s mass and atmosphere in Section 4, and give our conclusions in Section 5.

2. Observations and Archival Data

In this section we present the observations used to confirm the small habitable-zone planet TOI-700 d. In our analysis, we include the TESS discovery data and follow-up observations from Spitzer and the Las Cumbres Observatory (LCO). In the companion to this paper, Gilbert et al. (2020) characterize the TOI-700 system and validate the planets using a wealth of additional follow-up observations including multiple spectroscopic observations, high-spatial-resolution speckle imaging, and ground-based time-series photometry. An additional companion paper, Suissa et al. (2020), explore plausible atmospheres for TOI-700 d and the prospects for observing its atmosphere with future facilities. For brevity, we only describe the observations that directly feed into our EXOFASTv2 global analysis. See Table 1 for the magnitudes and kinematics in the literature.

2.1. TESS Photometry

TESS observed TOI-700 between 2018 July 25 and 2019 July 17. Because TOI-700 is located near the southern ecliptic pole, it fell in a region of sky that was observed nearly continuously by TESS. In total, TOI-700 was observed during 11 TESS sectors. Though TOI-700 is a nearby, bright dwarf star, it was not originally preselected for high-cadence TESS observations because of incorrect catalog stellar parameters. It was, however, proposed as part of Guest Investigator proposal G011180 (PI Dressing), so pixel time series from a small region of the TESS CCD near TOI-700 were downlinked with two-minute sampling.

After the data were downlinked, they were reduced and analyzed by the Science Processing Operations Center (SPOC) pipeline, based at the NASA Ames Research Center (Jenkins et al. 2016). The SPOC pipeline applies pixel-level calibrations to the data, identifies optimal photometric apertures, estimates flux contamination from other nearby stars, and extracts light curves. Instrumental artifacts are identified and removed from the light curves using the Presearch Data Conditioning (PDC) module (Smith et al. 2012; Stumpe et al. 2014). The processed light curves were searched for transits with the SPOC Transiting Planet Search (Jenkins 2002).

Early searches of the TOI-700 TESS light curves (both single sector and sectors 1–3) revealed some evidence for planetary transits, but these signals were not initially considered to be compelling enough to be promoted to the status of a planet candidate in the TESS Object of Interest (TOI) catalog (N. Guerrero et al. 2020, in preparation). After data from TESS sectors 1–6 were searched together, two planet candidates with 16.05 and 37.42 day periods were detected and released in the online TOI catalog. A third planet candidate with a period of 9.98 days was detected in a subsequent search of data from TESS sectors 1–9, and a final search of the TESS full first-year data set (11 sectors in total; see Figure 1) confirmed the detections (Twicken et al. 2018; Li et al. 2019).

These three candidates were investigated and characterized in detail by Gilbert et al. (2020), who statistically validated all three candidates as exoplanets. We note that it was more difficult to validate the planetary nature of the outer 37 day

Table 1
Properties of TOI-700

Other Identifiers			
TIC 150428135			
2MASS J06282325–6534456			
WISE J062823.05–653443.7			
Parameter	Description	Value	Source
α_{J2000}	Right ascension (R.A.)	06:28:23.22878	1
δ_{J2000}	Declination (decl.)	−65:34:45.52157	1
l	Galactic longitude	275°4682095	1
b	Galactic latitude	−26°8810581	1
l	Ecliptic longitude	275°4691	1
b	Ecliptic latitude	−26°8807	1
G	Gaia G mag.	12.0665 ± 0.0005	1
J	2MASS J mag.	9.469 ± 0.023	2
H	2MASS H mag.	8.893 ± 0.027	2
K_s	2MASS K_s mag.	8.634 ± 0.023	2
WISE1	WISE1 mag.	8.511 ± 0.023	3
WISE2	WISE2 mag.	8.387 ± 0.02	3
WISE3	WISE3 mag.	8.289 ± 0.016	3
WISE4	WISE4 mag.	8.267 ± 0.083	3
μ_α	Gaia DR2 proper motion in R.A. (mas yr ^{−1})	−102.75 ± 0.05	1
μ_δ	Gaia DR2 proper motion in decl. (mas yr ^{−1})	161.80 ± 0.06	1
π^b	Gaia parallax (mas)	32.18 ± 0.0392 ^a	1
d	Distance (pc)	31.075 ± 0.038 ^b	1
Spec. Type	Spectral type	M2V ± 1	4

Notes. The uncertainties of the photometry have a systematic error floor applied.

^a The R.A. and decl. are in epoch J2000. The coordinates come from Vizier, where the Gaia R.A. and decl. have been precessed to J2000 from epoch J2015.5.

^b Values have been corrected for the −0.82 μ s offset as advocated by Stassun & Torres (2018).

References. (1) Gaia Collaboration et al. (2018), (2) Cutri et al. (2003), (3) Cutri et al. (2014), (4) Gilbert et al. (2020).

period planet candidate around TOI-700. The transit signal was detected by TESS on only eight occasions and was fairly weak with a Multiple Event Statistic (a proxy for signal-to-noise ratio used by the SPOC pipeline) of 9.3. Experience from the Kepler mission has shown that a significant fraction of planet candidates in the low signal-to-noise-ratio/few-transit regime are false positives (Mullally et al. 2018; Burke et al. 2019). Although Gilbert et al. (2020) showed that the false-positive probability of TOI-700 d (including instrumental false alarms) was below the threshold required for statistical validation, a small possibility remained that TOI-700 d was spurious. Given the potential impact of the discovery, the likelihood that TOI-700 d will be the target of future observations, and the fact that we are still working to fully understand systematic errors in TESS data, we wanted an independent confirmation of the planet from another facility. We therefore proposed observations with the Spitzer Space Telescope to confirm the planet by detecting a transit at the predicted time.

2.2. LCOGT Photometry of TOI-700 c

As part of the TESS Follow-up Observing Program (TFOP), a transit of TOI-700 c was observed on 2019 November 1 in the z' band using one of the 1.0 m Las Cumbres Observatory Global Telescope Network (LCOGT) telescopes located at the South African Astronomical Observatory (SAAO; Brown et al. 2013).³⁰ The telescope is a Ritchey–Chrétien Cassegrain with a 4k × 4k Sinistro CCD with a 27' × 27' field of view and a 0''39 pixel scale. The observations were scheduled using the TESS Transit Finder that is built from the Tapir software tool (Jensen 2013). The observations were reduced and the light curves were extracted using the AstroImageJ software package (Collins et al. 2017). The photometry was extracted using a 3''9 aperture, as smaller apertures resulted in a significantly higher rms noise level. See Figure 2 for the plot of the LCOGT transit of TOI-700 c.

2.3. Spitzer Photometry of TOI-700 d

Two follow-up transits of TOI-700 d were observed with the Spitzer InfraRed Array Camera (IRAC; Fazio et al. 2004) on 2019 October 22 and 2020 January 5 as part of a Director's Discretionary Time (DDT) proposal award (program number 14314; PI Vanderburg). Each observation was 8.9 hours in duration, with a two-second exposure time, and used Channel 2 on IRAC, which is equivalent to a photometric wavelength range of 4–5 μ m. Prior to the observations of TOI-700, a 30 minute burn-in sequence was conducted to allow the spacecraft to thermally equilibrate and the detector to asymptote to a steady state of charge trapping and release. For both the burn-in sequence and the time-series observations, TOI-700 was placed on the detector on a pixel that is known to have minimal sensitivity variations.

We downloaded the Spitzer observations from the archive and reduced the Basic Calibrated Data (BCD, provided by the Spitzer Science Center) using the custom aperture photometry routine developed by Cubillos et al. (2013). This analysis package (which is available open source on GitHub³¹) fits a 2D Gaussian profile to the stellar image in each Spitzer exposure after upsampling by a factor of 5 in each spatial direction. We identified and masked pixels with outlying values using an iterative sigma-clipping procedure and then summed the flux in each fixed aperture. We tested apertures with radii ranging from 2 to 4 pixels in 0.25 pixel steps and found that a radius of 3.0 pixels minimizes the noise in each of the extracted light curves. An annulus with an inner radius of 7 pixels and outer radius of 15 pixels was adopted for the determination of the median background value.

The dominating systematics for the 4.5 μ m Spitzer channel are intrapixel sensitivity variations (Charbonneau et al. 2005). We therefore fitted for them by using the BiLinearly Interpolated Subpixel Sensitivity (BLISS) map technique introduced by Stevenson et al. (2012). We describe the full Spitzer light curve, $F(x, y, X, Y, t)$, by

$$F(x, y, X, Y, t) = F_s R(t) M(x, y) T(t) G(X, Y, t), \quad (1)$$

where F_s is the constant out-of-transit flux, $R(t)$ is the ramp model, $M(x, y)$ is the BLISS map with (x, y) describing the position of

³⁰ <https://lco.global>

³¹ <https://github.com/kevin218/POET>

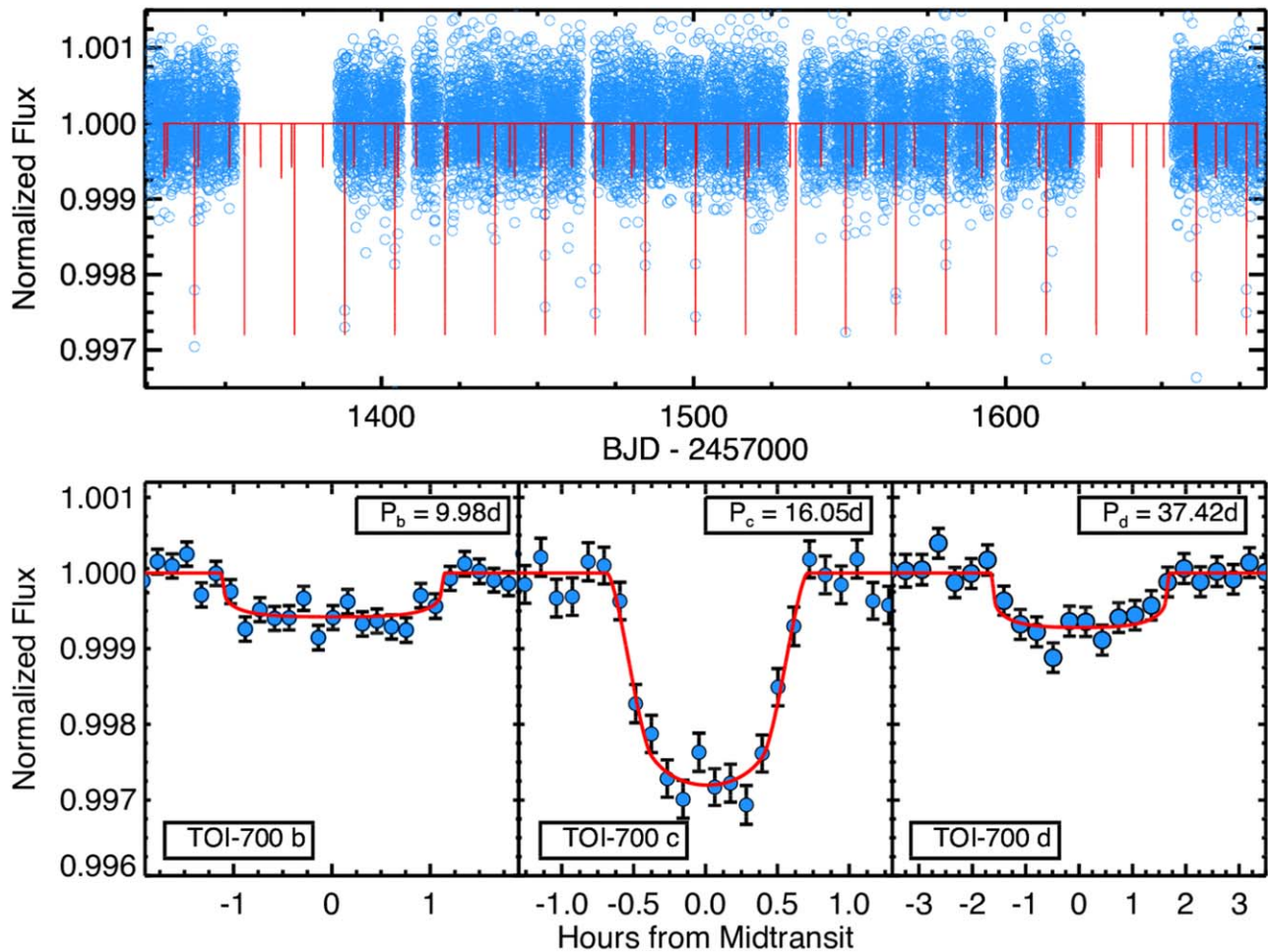


Figure 1. Photometric observations of the TOI-700 system. The light curve has been processed to remove stellar variability and instrumental systematics. Top panel: the blue open circles are the TESS observations binned to 30 minutes for all 11 sectors of TESS. Because TOI-700 falls near TESS’s continuous viewing zone, there are almost 10 months of data. Bottom panels: the TESS transits for (left) TOI-700 b, (middle) TOI-700 c, and (right) TOI-700 d phase-folded to the best-fit ephemeris from the global fit (see Section 3). The TESS observations have been binned for visual clarity. The EXOFASTv2 transit model is shown in red in each panel.

(The data used to create this figure are available.)

the star on the detector, $T(t)$ is the Mandel & Agol (2002) transit model implemented in BATMAN (Kreidberg 2015), and $G(X, Y, t)$ is a term fitting for variations in the pixel response function (PRF) using a 2D cubic with the Gaussian widths (X, Y) .

An initial fit with the BLISS map model revealed a clear transit in each of the Spitzer light curves with the same depth and duration seen in the TESS light curve. After detecting the transits, we adjusted our systematics correction to further optimize the Spitzer light curve. The optimal resolution for BLISS mapping was found to be 0.01 pixels for the first observation and 0.008 pixels for the second. We also experimented with the complexity of the light-curve model. In order to compare models with different numbers of free parameters, we used the Bayesian Information Criterion (BIC; Schwarz 1978; Liddle 2007). Combinations of a linear ramp $R(t)$ and PRF fits $G(X, Y, t)$ of different orders were tested. A significant increase in the BIC for those models showed that these more complex models are not justified.

Our final model consisted only of the BLISS map, a constant, and the BATMAN transit model. The latter has the following parameters: T_0 , R_p/R_* , P , a/R_* , $\cos i$, e , ω_* , u_1 , and

u_2 (see Table 2 for a description of these parameters). As multiple transits were observed with TESS and only two with Spitzer, we fixed the period P to the value determined by TESS.

Finally, we compared the Spitzer model with a fit that fixes the system-specific parameters $(P, a/R_*, \cos i)$ to values from a fit of the TESS observations using only EXOFASTv2. Both of these cases reproduce transit depths that are consistent with each other. The final fitted $4.5 \mu\text{m}$ light curves from Spitzer with the EXOFASTv2 global model are shown in Figure 3. Spitzer independently detected the transit of TOI-700 d with 12σ confidence.

In order to account for the correlated noise in our light curves, we calculate β using the “time-averaging” method (Pont et al. 2006; Winn et al. 2007). It scales the standard deviation of the data set with a factor β , which denotes the ratio between the actual achieved standard deviation of the binned residuals and the standard deviation in the absence of red noise. By taking median values of this ratio for binnings between 15 and 30 minutes following Winn et al. (2008), we estimate $\beta_1 = 1.268$ for the first observation and $\beta_2 = 1.210$ for the second.

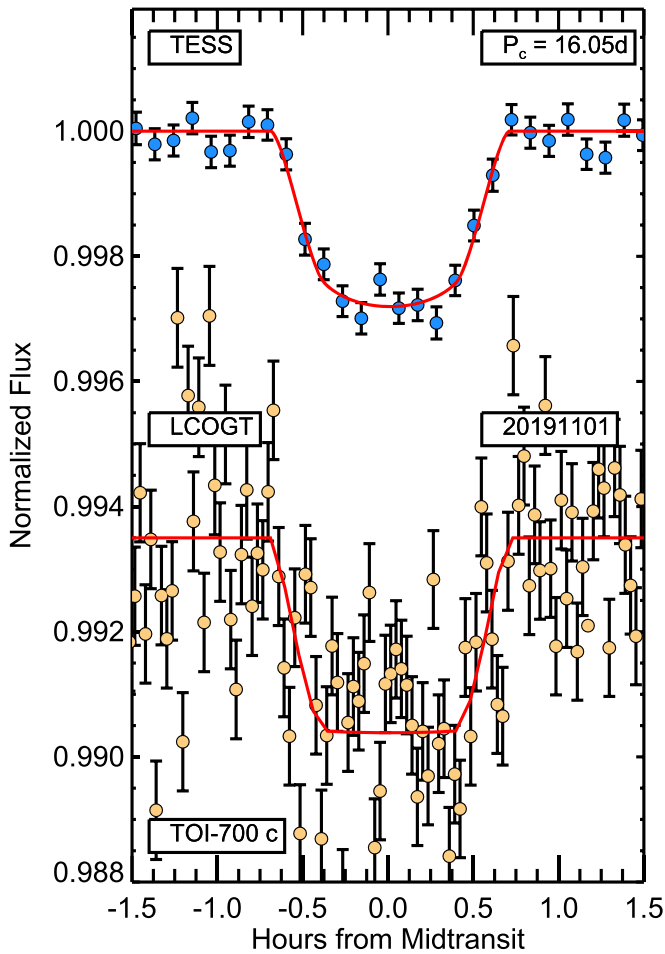


Figure 2. Photometric observations of TOI-700 c from TESS and LCO (2019 November 1). The TESS and LCO observations have been binned for visual clarity. The EXOFASTv2 transit model for each data set is shown in red for each observation.

(The data used to create this figure are available.)

3. EXOFASTv2 Global Fits

To determine the full system parameters, and especially those of the habitable-zone Earth-sized planet, TOI-700 d, we globally fit the photometric observations from 11 sectors of TESS, the observations from Spitzer, and a follow-up transit of TOI-700 c from the Las Cumbres Observatory using EXOFASTv2 (Eastman et al. 2013, 2019). We removed low-frequency variability from the TESS light curves by fitting the light curves with basis splines (with a 1.5 day knot spacing), ignoring points during the transits of the three planets, and iteratively excluding outliers (see Figure 3 from Vanderburg & Johnson 2014). For computational efficiency, we averaged the two-second cadence Spitzer light curve into one-minute bins. The Spitzer light curve had been corrected for systematics as described in Section 2.3.

EXOFASTv2 models planetary systems self-consistently, so the transit parameters of each planet, TOI-700 b, c, and d were fit simultaneously with, and informed by, their host star’s parameters. Because TOI-700 is a low-mass dwarf star, the stellar evolutionary and stellar atmospheric models embedded within EXOFASTv2 are not reliable. Therefore, we use the

absolute K -mag relations from Mann et al. (2015, 2019) to determine the mass and radius of TOI-700 and use these values with a conservative 5% uncertainty as Gaussian priors on R_* and M_* of $0.419 \pm 0.021 R_\odot$ and $0.417 \pm 0.021 M_\odot$. We note that these values are well within 1σ of the mass and radius used for TOI-700 from Gilbert et al. (2020). We do not use the Claret (2017) limb-darkening tables within the global fit to constrain u_1 and u_2 , and instead leave the limb-darkening parameters to be constrained by the transit light curves in each bandpass, as well as EXOFASTv2’s built-in uniform prior that only allows steps within the physical bounds identified by Kipping (2013) for any band: $u_1 + u_2 < 1$, $u_1 > 0$, and $u_1 + 2u_2 > 0$. We also place priors on T_{eff} (3460 ± 65 K) and $[\text{Fe}/\text{H}]$ (-0.07 ± 0.11 dex) from an analysis of spectroscopic observations using the Southern Astrophysical Research Telescope combined with a spectral energy distribution analysis (see Gilbert et al. 2020). Because priors are placed on M_* and R_* , the corresponding priors on T_{eff} and $[\text{Fe}/\text{H}]$ do not affect the fitted planet parameters and are only used to derive quantities such as L_* and T_{eq} , along with the predicted Spitzer 3.6 and 4.5 μm eclipse depths shown in Table 2. To account for the possible correlated noise in the Spitzer observations, we have modified the per-point error for each Spitzer light curve following Winn et al. (2008). Specifically, the per-point errors on the Spitzer light curves are derived by multiplying the β parameter calculated for each Spitzer light curve (see Section 2.3) and the light-curve rms. See the Figures 1–3 light-curve plots of TESS, LCOGT, and Spitzer with the EXOFASTv2 models.

Because we are simultaneously modeling photometric data for TOI-700 d from different observatories, we performed some experiments to ensure that the data from TESS and Spitzer were consistent and neither significantly biased the transit depth. We do not perform these tests on the LCOGT observations because the LCOGT observations are far less precise. We tested the TESS and Spitzer data sets for consistency by jointly fitting the two light curves, allowing for a dilution term in either data set while using the other as the baseline for comparison. Fitting for a dilution term in one bandpass effectively decoupled the measured transit depth from the two observatories. In all cases, the fit results were consistent with no significant additional dilution needed—in other words, the transit depth measured by TESS was consistent with that measured by Spitzer. This is not surprising given that the SPOC pipeline accounts for blending from nearby stars in the TESS data and that none of our follow-up observations, including the Spitzer images and high-spatial-resolution speckle observations, show evidence of any unknown additional stellar companions close enough to contaminate the Spitzer photometry.

4. Discussion

TOI-700 is a compelling system for future characterization observations thanks to its relative proximity ($d = 31.075 \pm 0.038$ pc) and brightness ($H = 8.893 \pm 0.027$). All three planets orbiting TOI-700 are sub-Neptune in size ($R_b = 1.037^{+0.065}_{-0.064} R_\oplus$, $R_c = 2.65^{+0.16}_{-0.15} R_\oplus$, and $R_d = 1.144^{+0.062}_{-0.061} R_\oplus$), and orbit with periods of 9.977, 16.0511, and 37.425 days. We note that the ratio of the planet’s orbital periods is 1.608 for c:b, and the d:c ratio is 2.33. These ratios are within 1% of an 8:5 resonance c:b and 7:3 for d:c. See Section 6.3 of Gilbert et al. (2020), which presents a detailed transit timing and photodynamical analysis. Their results suggest minimal perturbations on the

Table 2
Median values and 68% Confidence Interval for the Global Model of TOI-700

Parameter	Description (Units)	Values		
Stellar Parameters:				
M_*	Mass (M_\odot)	0.415 ± 0.020		
R_*	Radius (R_\odot)	0.424 ± 0.017		
L_*	Luminosity (L_\odot)	0.0232 ^{+0.0027} _{-0.0025}		
ρ_*	Density (cgs)	7.68 ^{+1.0} _{-0.89}		
log g	Surface gravity (cgs)	4.802 ^{+0.038} _{-0.039}		
T_{eff}	Effective temperature (K)	3461 ± 66		
[Fe/H]	Metallicity (dex)	−0.07 ± 0.11		
Planetary Parameters:				
		b	c	d
P	Period (days)	9.97702 ^{+0.00024} _{-0.00028}	16.051110 ^{+0.000062} _{-0.000063}	37.42475 ^{+0.00036} _{-0.00040}
R_p	Radius (R_\oplus)	1.037 ^{+0.065} _{-0.064}	2.65 ^{+0.16} _{-0.15}	1.144 ^{+0.062} _{-0.061}
T_C	Time of conjunction (BJD _{TDB})	2458331.3537 ^{+0.0059} _{-0.0032}	2458340.08813 ± 0.00095	2458330.4754 ^{+0.0047} _{-0.0041}
T_0^a	Optimal conjunction time (BJD _{TDB})	2458490.9867 ^{+0.0027} _{-0.0029}	2458548.75256 ± 0.00050	2458742.1476 ^{+0.0016} _{-0.0012}
a	Semimajor axis (au)	0.0677 ± 0.0011	0.0929 ± 0.0015	0.1633 ^{+0.0026} _{-0.0027}
i	Inclination (degrees)	89.66 ^{+0.24} _{-0.29}	88.868 ^{+0.083} _{-0.10}	89.79 ^{+0.14} _{-0.12}
e	Eccentricity	0.081 ^{+0.095} _{-0.058}	0.078 ^{+0.075} _{-0.056}	0.111 ^{+0.14} _{-0.078}
ω_*	Argument of periastron (degrees)	−75 ⁺⁹⁴ ₋₈₄	81 ⁺⁸⁰ ₋₈₃	0 ⁺¹⁴⁰ ₋₁₃₀
T_{eq}	Equilibrium temperature (K)	417 ± 12	356 ± 10.	268.8 ^{+7.7} _{-7.6}
R_p/R_*	Radius of the planet in stellar radii	0.0224 ^{+0.0010} _{-0.0011}	0.0573 ^{+0.0020} _{-0.0018}	0.02476 ^{+0.00088} _{-0.00089}
a/R_*	Semimajor axis in stellar radii	34.3 ^{+1.5} _{-1.4}	47.1 ^{+2.0} _{-1.9}	82.9 ^{+3.5} _{-3.3}
δ	Transit depth (fraction)	0.000503 ^{+0.000048} _{-0.000046}	0.00329 ^{+0.00024} _{-0.00020}	0.000613 ^{+0.000045} _{-0.000043}
$Depth$	Flux decrement at midtransit	0.000503 ^{+0.000048} _{-0.000046}	0.00329 ^{+0.00024} _{-0.00020}	0.000613 ^{+0.000045} _{-0.000043}
τ	Ingress/egress transit duration (days)	0.00220 ^{+0.00029} _{-0.00017}	0.0138 ^{+0.0026} _{-0.0023}	0.00367 ^{+0.00078} _{-0.00032}
T_{14}	Total transit duration (days)	0.0943 ^{+0.0056} _{-0.0049}	0.0589 ^{+0.0019} _{-0.0018}	0.1384 ^{+0.0033} _{-0.0027}
T_{FWHM}	FWHM transit duration (days)	0.0920 ^{+0.0055} _{-0.0048}	0.0451 ^{+0.0020} _{-0.0023}	0.1345 ^{+0.0031} _{-0.0027}
b	Transit impact parameter	0.21 ^{+0.19} _{-0.15}	0.893 ^{+0.017} _{-0.021}	0.30 ^{+0.19} _{-0.20}
b_S	Eclipse impact parameter	0.20 ^{+0.15} _{-0.14}	0.951 ^{+0.14} _{-0.074}	0.30 ^{+0.12} _{-0.19}
τ_S	Ingress/egress eclipse duration (days)	0.00205 ± 0.00023	0.0141 ^{+0.0078} _{-0.014}	0.00366 ^{+0.00041} _{-0.00038}
$T_{S,14}$	Total eclipse duration (days)	0.0888 ^{+0.0075} _{-0.0095}	0.052 ^{+0.011} _{-0.052}	0.138 ^{+0.015} _{-0.016}
$T_{S,\text{FWHM}}$	FWHM eclipse duration (days)	0.0867 ^{+0.0074} _{-0.0093}	0.026 ^{+0.023} _{-0.026}	0.134 ^{+0.015} _{-0.016}
$\delta_{S,3.6 \mu\text{m}}$	Blackbody eclipse depth at 3.6 μm (ppm)	0.068 ^{+0.020} _{-0.017}	0.085 ^{+0.031} _{-0.024}	0.00039 ^{+0.00019} _{-0.00013}
$\delta_{S,4.5 \mu\text{m}}$	Blackbody eclipse depth at 4.5 μm (ppm)	0.358 ^{+0.085} _{-0.072}	0.63 ^{+0.18} _{-0.14}	0.0063 ^{+0.0024} _{-0.0018}
$\langle F \rangle$	Incident flux ($10^9 \text{ erg s}^{-1} \text{ cm}^{-2}$)	0.00681 ^{+0.00083} _{-0.00077}	0.00362 ^{+0.00043} _{-0.00039}	0.00116 ^{+0.00014} _{-0.00013}
T_p	Time of periastron (BJD _{TDB})	2458327.3 ^{+3.1} _{-2.8}	2458324.0 ^{+3.3} _{-3.1}	2458297 ^{+10.} ₋₁₂
T_S	Time of eclipse (BJD _{TDB})	2458326.36 ^{+0.49} _{-0.51}	2458332.07 ^{+0.73} _{-0.68}	2458311.8 ^{+3.3} _{-3.2}
T_A	Time of ascending node (BJD _{TDB})	2458328.80 ^{+0.23} _{-0.44}	2458336.23 ^{+0.56} _{-0.34}	2458321.1 ^{+1.7} _{-2.1}
T_D	Time of descending node (BJD _{TDB})	2458333.90 ^{+0.44} _{-0.24}	2458343.96 ^{+0.34} _{-0.55}	2458339.8 ^{+2.1} _{-1.7}
$e \cos \omega_*$		−0.000 ^{+0.078} _{-0.080}	0.000 ^{+0.071} _{-0.067}	0.00 ± 0.14
$e \sin \omega_*$		−0.027 ^{+0.043} _{-0.085}	0.031 ^{+0.077} _{-0.044}	−0.001 ^{+0.056} _{-0.086}
$M_p \sin i$	Minimum mass (M_\oplus)	1.25 ^{+1.00} _{-0.35}	7.9 ^{+2.7} _{-1.8}	1.94 ^{+0.69} _{-0.57}
M_p/M_*	Mass ratio	0.0000091 ^{+0.0000073} _{-0.0000025}	0.000057 ^{+0.000020} _{-0.000013}	0.0000140 ^{+0.0000051} _{-0.0000041}
d/R_*	Separation at midtransit	35.1 ^{+3.5} _{-2.5}	45.3 ^{+3.6} _{-4.3}	82.2 ^{+7.9} _{-7.6}
Wavelength Parameters:				
		z'	4.5 μm	TESS
u_1	Linear limb-darkening coefficient	0.36 ^{+0.36} _{-0.25}	0.128 ^{+0.19} _{-0.095}	0.20 ^{+0.12} _{-0.11}
u_2	Quadratic limb-darkening coefficient	0.02 ^{+0.31} _{-0.26}	0.08 ^{+0.24} _{-0.14}	0.48 ± 0.13
A_D	Dilution from neighboring stars	−0.000 ± 0.011

Table 2
(Continued)

Parameter	Description (Units)	Values			
Transit Parameters:		TESS	Spitzer 20191022 (4.5 μm)	LCO SAAO 20191101 (z')	Spitzer 20200105 (4.5 μm)
σ^2	Added variance	$0.000000091^{+0.000000036}_{-0.000000035}$	$0.000000050^{+0.000000082}_{-0.000000038}$	$0.0000266^{+0.00000042}_{-0.00000037}$	$0.000000048^{+0.000000079}_{-0.000000036}$
F_0	Baseline flux	$1.000072^{+0.000017}_{-0.000016}$	$1.000063^{+0.000040}_{-0.000041}$	0.99989 ± 0.00017	$1.000078^{+0.000041}_{-0.000040}$

Notes. See Table 3 in Eastman et al. (2019) for the definition and explanation of the derived and fitted parameters in EXOFASTv2. Equilibrium temperature is calculated assuming zero albedo and perfect heat redistribution: $T_{\text{eq}} = T_{\text{eff}} \sqrt{\frac{R_p}{2a}}$. The derived secondary eclipse depths assume a Bond albedo of zero.

^a Minimum covariance with period. All values in this table for the secondary occultation of TOI-700 b are the predicted values from our global analysis.

orbit of planet d from planets b and c. We see no evidence of transit timing variations in the combined Spitzer and TESS global fit, supporting their result. We also see a slight midtransit brightening during the Spitzer observations of TOI-700 d. However, because it is similar in amplitude to other features in the light curve, not seen in the TESS observations, and that there is correlated noise in the Spitzer data, we do not believe it to be astrophysical in origin. We direct the reader to Gilbert et al. (2020) for a detailed analysis and discussion of the TOI-700 system as a whole (and the validation of all three planets in the system), and we focus the rest of our discussion on TOI-700 d, the first habitable-zone Earth-sized planet from NASA’s TESS mission.

4.1. Spitzer Confirmation of TOI-700 d

While Gilbert et al. (2020) were able to rule out most false-positive scenarios for TOI-700 d, a small probability remained that the planet was not real. Our Spitzer observations rule out many of the remaining false-positive scenarios for the planet candidate. Most importantly, we have now detected TOI-700 d’s transit with two different telescopes, so systematic errors in the TESS light curve cannot be the source of the signal. Given TOI-700 d’s relatively low detection significance and small number of observed transits, instrumental artifacts were the greatest uncertainty in the validation of TOI-700 d. The Spitzer observations have retired this risk.

Spitzer also showed that the transit of TOI-700 d is achromatic, which constrains blended companions and rejects additional astrophysical false-positive scenarios. We measured the transit depths (R_p^2/R_*^2) in the TESS and Spitzer bandpasses by fitting the light curves simultaneously with Mandel & Agol (2002) models using an affine invariant Markov Chain Monte Carlo sampler (Goodman & Weare 2010). We found that the Spitzer transit (612 ± 44 ppm) is slightly shallower than the TESS signal (677 ± 98 ppm). We constrained red contaminants by comparing the measured ratio of the Spitzer/TESS depths ($0.90^{+0.14}_{-0.12}$) to the expected ratios for a variety of cooler companions using Equation (5) from Désert et al. (2015) and MIST isochrones (Choi et al. 2016). We rule out blends with very red, comoving stars with mass less than $0.30 M_\odot$ (95% confidence). The Spitzer observations eliminate almost all remaining false-positive scenarios for TOI-700 d, especially instrumental artifacts. These data, combined with the observations and statistical validation presented by Gilbert et al. (2020), allow us to confidently pursue future observations.

4.2. Spitzer Improvement on the Parameters of TOI-700 c and d

From our joint TESS and Spitzer global fit, we are able to improve the properties of TOI-700 d, relative to the results of an EXOFASTv2 fit that only included the TESS observations. This is similar to the fit that is presented in Gilbert et al. (2020), except that they used the exoplanet software package (Foreman-Mackey & Barentsen 2019). This comparison removes any concern that any observed differences or improvements are caused by the analysis methodology. The Spitzer observations took place on 2019 October 22 and 2020 January 5, 99 and 174 days after the end of the 11 TESS sectors in which TOI-700 was observed (2019 July 17), extending the total time baseline of observations by 49%. The combined Spitzer transits are detected at $\sim 14\sigma$ while the TESS combined transits are detected at 7σ . This expansion in the photometric baseline yielded a 61% improvement on the average precision on TOI-700 d’s orbital period. Additionally, thanks to its infrared capability (ideal for M dwarfs like TOI-700) and larger aperture compared to TESS, Spitzer was able to reduce the uncertainty in R_p/R_* for TOI-700 d by 39%. Our analysis also included a transit of TOI-700 c from LCOGT on 2019 November 01, 108 days after the end of the 11 sectors of TESS. Our analysis shows a 32% improvement on the precision of TOI-700 c’s orbital period and a 9% improvement on the planet’s R_p/R_* .

The improved precision of these parameters will pay dividends as more follow-up observations of TOI-700 d are conducted. The improved orbital period measurement will help plan future transit observations of TOI-700 d more efficiently, and our more precise radius measurement will be critical for understanding the planet’s bulk composition. Decreasing radius uncertainties is particularly important for understanding the composition of rocky planets. For rocky planets (with some constant bulk iron/silicate abundance ratio), the planet’s mass m and radius r are related by $m \propto r^{3.6}$ (Zeng et al. 2016). This means that when inferring a rocky planet’s iron/silicate ratio, a planet’s radius must be known 3.6 times more precisely than its mass for the two observables to contribute equally. In other words, improving the radius precision will improve the ability of future RV observations to determine TOI-700 d’s bulk composition.

4.3. TOI-700’s Habitable Zone

The location of the habitable zone of planetary systems is calculated based on the premise that a planet similar to Earth could retain surface liquid water given sufficient atmospheric pressure (Kasting et al. 1993; Kane & Gelino 2012; Kopparapu et al. 2013, 2014). Such calculations are sensitive

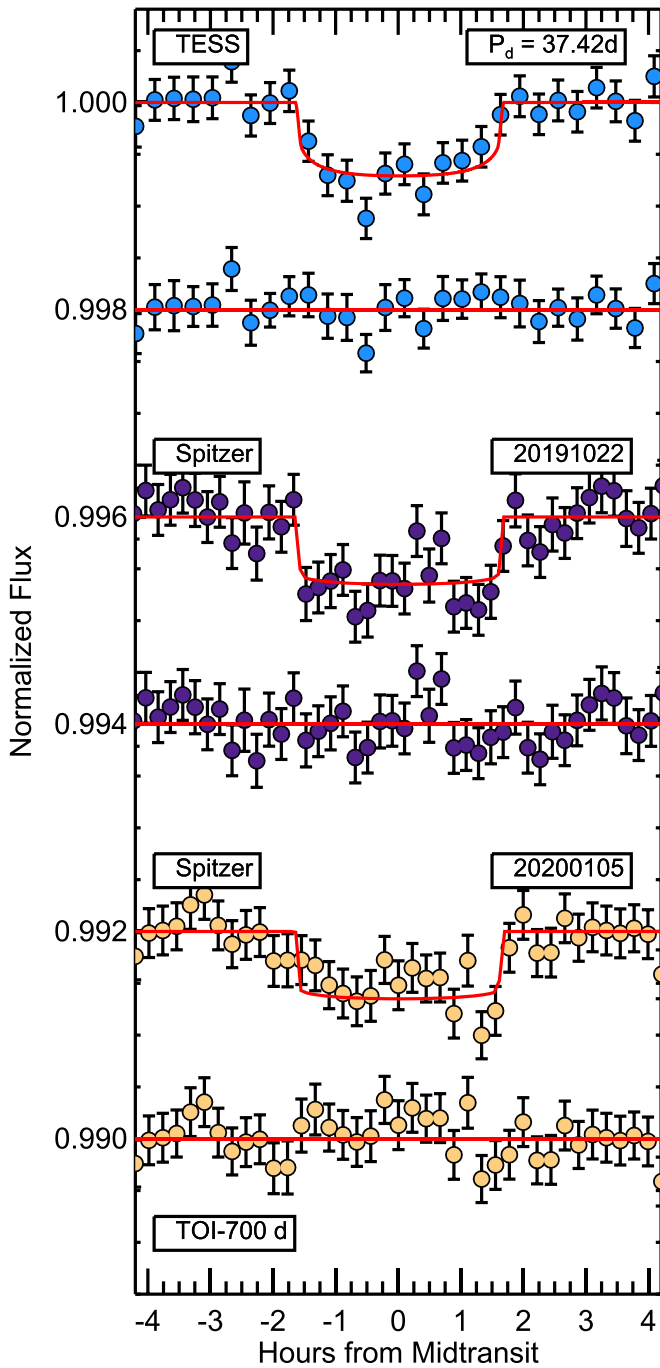


Figure 3. Photometric observations of TOI-700 d from TESS and Spitzer (2019 October 22 and 2020 January 5). The TESS and Spitzer observations have been binned for visual clarity. The EXOFASTv2 transit model for each data set is shown in red for each observation. The residuals of our model fit are shown below each light curve.

(The data used to create this figure are available.)

to the precision of the stellar parameters (Kane 2014, 2018), in particular the luminosity and effective temperature of the host star. Specifically, the habitable-zone boundaries are estimated using one-dimensional cloud-free climate models that monitor the change in surface radiative balance for an Earth analog as a function of incident flux at infrared wavelengths. For this purpose, we utilize Equations (4) and (5) along with the coefficients of Table 1 from Kopparapu et al. (2014) to calculate the habitable-zone boundaries. The

habitable zone is often described as either “conservative,” with boundaries of runaway greenhouse and maximum greenhouse, or “optimistic,” with boundaries determined from empirical assumptions of water prevalence on Venus and Mars (Kane et al. 2016). We use the stellar parameters shown in Table 2 to calculate the extent of the TOI-700 habitable zone for both the conservative and optimistic cases. Figure 4 shows a schematic of the TOI-700 system comparing the orbits of the planets to the location of the conservative and optimistic habitable zones. TOI-700 d’s orbit lies confidently within the conservative habitable zone and is small enough (only 20% larger than Earth) that it could be terrestrial (Rogers 2015; Wolfgang & Lopez 2015). It is worth noting the caveat that there are various effects that influence the boundaries of the habitable zone. In the case of tidal locking, calculations from climate models have demonstrated that this generally has the effect of widening the habitable zone (Yang et al. 2013, 2019). Based on estimates of tidal locking timescales by Barnes (2017), the majority of habitable-zone terrestrial planets discovered by TESS are expected to be tidally locked for ages less than ~ 1 Gyr, therefore increasing the confidence in the habitable-zone status of TOI-700 d.

4.4. Known Habitable-zone Terrestrial-sized Planets

TOI-700 d joins a very small population of presently known habitable-zone terrestrial-sized planets. In this subsection, we compare TOI-700 d to a sample of habitable-zone planets very similar in size to Earth. Starting from a list of known small habitable-zone planets,³² we identify planets smaller than $1.5 R_{\oplus}$, the radius below which hot planets orbiting M dwarfs similar to TOI-700 ($0.415 \pm 0.021 M_{\odot}$) tend to have rocky compositions (Rogers 2015; Fulton et al. 2017; Cloutier & Menou 2020). After this cut, we are left with 10 small habitable-zone³³ planets: TRAPPIST-1 (d, e, f, and g; Gillon et al. 2017), Kepler-186 f (Quintana et al. 2014), Kepler-1229 b (Morton et al. 2016), Kepler-442 b (Torres et al. 2015), Kepler-62 f (Borucki et al. 2013), Kepler-1649c (Vanderburg et al. 2020; this was recently announced and not in the known list at the time of this paper), and TOI-700 d. We note that this cut removes all RV-only planets and LHS 1140 b ($1.73 R_{\oplus}$), which has a density consistent with a rocky composition (Dittmann et al. 2017; Ment et al. 2019). Of the remaining planets, TOI-700 d orbits the brightest host star by far. In the optical, TOI-700’s Gaia G -band magnitude (12.07) is 4.5 times brighter than the next brightest host (Kepler-62, $G = 13.72$), and in the near-infrared, TOI-700’s K -band magnitude (8.63) is 4.6 times brighter than the next brightest host (TRAPPIST-1, $K = 10.30$). TOI-700’s apparent brightness makes it particularly attractive among small habitable-zone planets for follow-up observations.

4.5. Future Radial Velocity Observations of TOI-700 d

Among small, habitable-zone planets, TOI-700 d is well suited for precise RV observations to measure its mass and confirm/rule out a rocky composition. Its host star is a quiet M dwarf ($0.415 M_{\odot}$) with no large photometric variations observed in the full TESS light curve. The host star appears to be relatively inactive with a long rotation period of 54 ± 0.8 days.

³² <http://phl.upr.edu/projects/habitable-exoplanets-catalog>

³³ K2-72 e and TRAPPIST-1 d orbit in their star’s optimistic habitable zones, while the others orbit within the conservative habitable zone.

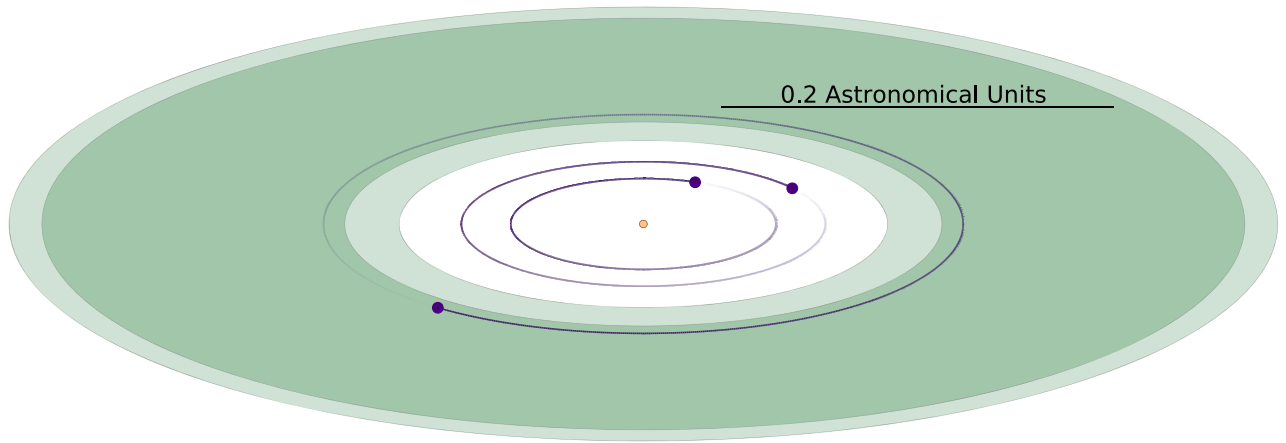


Figure 4. Schematic of the TOI-700 system, from the vantage of an observer inclined by 20° from the plane of the system, showing the orbits of the planets (faded purple lines), the conservative habitable zone (dark green), and the optimistic extension to the habitable zone (light green; Kasting et al. 1993; Kane & Gelino 2012; Kopparapu et al. 2013, 2014). The size of the star TOI-700 is shown to scale, but the sizes of the planets are not.

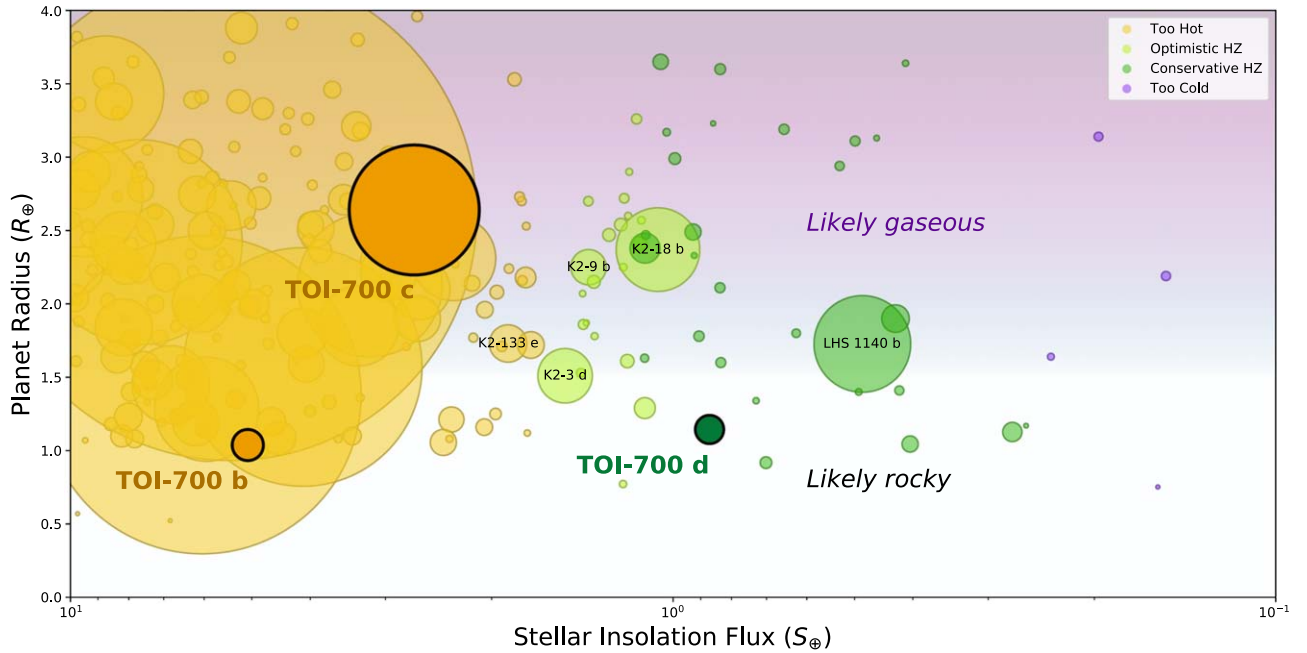


Figure 5. TOI-700 in the context of known exoplanets. Using data from the NASA Exoplanet Archive (Akeson et al. 2013), we plot the radius of known exoplanets vs. the incident flux they receive from their host stars. The symbols are color-coded based on their position relative to the circumstellar habitable zone, where yellow dots represent planets too hot to have liquid water, purple dots represent planets too cold to have liquid water, and light and dark green points represent planets in the optimistic and conservative habitable zones, respectively. The background shading indicates whether a planet is likely rocky or gaseous based on its size alone, following Rogers (2015; Wolfgang & Lopez 2015). We used the polynomial expressions from Kopparapu et al. (2014) to determine the boundaries of the optimistic and conservative habitable zones for each host star. The area of the symbol is inversely proportional to the amount of observing time required to measure the planet’s mass with radial velocity observations—larger points are easier measurements (see Section 4.5). In terms of RV accessibility, TOI-700 d stands out as one of the best habitable-zone planets with a radii small enough that they are likely rocky. We note that LHS 1140 b is more accessible based on our metrics and has a measured mass consistent with it being rocky (Dittmann et al. 2017; Ment et al. 2019).

With no signs of activity in the spectra and a rotation period that differs from the orbital period, TOI-700 should be well suited for RV follow-up (we direct the reader to Gilbert et al. 2020 for a thorough discussion on the stellar classification, including spectral analysis). Using the Chen & Kipping (2017) mass/radius relation,³⁴ our EXOFASTv2 model reports mass estimates for TOI-700 b, c, and d to be $M_b = 1.26^{+1.0}_{-0.35} M_\oplus$, $M_c = 7.8^{+2.7}_{-1.8} M_\oplus$, and $M_d = 2.10^{+0.68}_{-0.65} M_\oplus$, which correspond

to RV semi-amplitudes of $0.68^{+0.55}_{-0.19}$, $3.60^{+1.2}_{-0.82}$, and $0.73^{+0.24}_{-0.23} \text{ m s}^{-1}$. Figure 5 compares the RV accessibility of TOI-700 d to other known transiting exoplanets. The symbol size is inversely proportional to a simple metric estimating the amount of observing time required to detect each planet’s RV signal (assuming the Weiss & Marcy 2014 mass/radius relation):

$$\text{Point Size} \propto K^2 \times 10^{-0.4G} \quad (2)$$

where K is the semi-amplitude and G is the Gaia G -band magnitude of the host star. By this metric, TOI-700 d is the best small habitable-zone (conservative) planet ($R_p < 1.5 R_\oplus$) for RV

³⁴ If we adopt the Weiss & Marcy (2014) mass–radius relation, we get similar masses for each planet: $M_b = 1.1 M_\oplus$, $M_c = 6.7 M_\oplus$, and $M_d = 2.2 M_\oplus$.

observations. Detecting the RV signal of TOI-700 d will be challenging but is within the current capabilities of the most precise spectrographs like the Echelle SPectrograph for Rocky Exoplanets and Stable Spectroscopic Observations (ESPRESSO) on the Very Large Telescope (VLT) (Pepe et al. 2010). ESPRESSO is stable enough to detect the planet’s $\approx 80 \text{ cm s}^{-1}$ signal, and TOI-700 is bright enough that ESPRESSO should achieve $\approx 70 \text{ cm s}^{-1}$ photon-limited precision in 1 hr exposures (Pepe et al. 2014; Faria et al. 2020, and J. P. Faria 2020, private communication).

4.6. Future Atmospheric Characterization of TOI-700 d

Despite its favorable properties, TOI-700 d will be a challenging target for transit spectroscopy observations to search for biosignatures or other molecules in its atmosphere in the near future. To assess the feasibility of detecting these features, we simulated JWST spectra for the planet (assuming Earth-like and CO_2 -dominated atmospheres) with Pandexo (Batalha et al. 2017) using the NIRSpec/G235M observing mode. This mode provides the highest signal-to-noise ratio for the transmission spectra of rocky planets around M dwarfs (Morley et al. 2017). Assuming photon-noise-limited observations, distinguishing such features from a featureless spectrum at 5σ confidence would require data spanning more than 200 transits ($\gtrsim 1000 \text{ hr}$), equivalent to observing every single transit of TOI-700 d for the first 20 yr after JWST’s launch. It would also require an order of magnitude higher precision on the transit depth measurements than has ever been achieved (Line et al. 2016). TOI-700 d requires significantly more observing time than the TRAPPIST-1 planets because of the relatively small planet-to-star radius ratio. We direct the reader to Paper III in this series, which does a much more in depth analysis of TOI-700 d’s possible atmosphere, including a 3D general circulation model of plausible atmospheres and their detectability using future observatories (Suissa et al. 2020). While follow-up JWST observations are not practical, the discovery of this planet motivates the development of future large-aperture observing facilities capable of sub-10 ppm measurement precision in the near-infrared.

5. Conclusion

We present new Spitzer observations confirming the planetary nature of the TOI-700 d, a habitable-zone Earth-sized planet located within a multiplanet system. TOI-700 is a early-M dwarf ($M_\star = 0.415 \pm 0.020 M_\odot$ and $R_\star = 0.424 \pm 0.017 R_\odot$) located 31.1 pc from the Sun. Using a combination of high-spatial-resolution speckle imaging, spectroscopic observations from CHIRON, and ground-based seeing-limited photometry from the TESS Followup Observing Program (TFOP), Gilbert et al. (2020) were able to statistically validate the planetary nature of TOI-700 b, c, and d. Although the calculated false-positive probability was low enough for the planet to be statistically validated, we sought independent transit confirmation with Spitzer given the importance of the discovery and the relatively low signal-to-noise ratio of the transit signal from TESS. Our $4.5 \mu\text{m}$ Spitzer observations conclusively confirmed the transit of TOI-700 d, ruling out any remaining instrumental origin for the signal and solidifying its validation.

We model the TESS and Spitzer photometry to determine the full system parameters. TOI-700 hosts two Earth-sized planets and a sub-Neptune ($R_b = 1.044^{+0.065}_{-0.063} R_\oplus$, $R_c = 2.64^{+0.16}_{-0.14} R_\oplus$, and $R_d = 1.220^{+0.073}_{-0.063} R_\oplus$) with periods of $P_b = 9.97702^{+0.00024}_{-0.00028}$

$P_c = 16.051108^{+0.000062}_{-0.000064}$, and $P_d = 37.42469^{+0.00033}_{-0.00042}$ days. TOI-700 d is located well within the conservative habitable zone for its host star and is the first habitable-zone Earth-sized planet discovered from NASA’s TESS mission. TOI-700 is the brightest known host of a transiting habitable-zone Earth-sized planet discovered to date.

Although atmospheric characterization is likely out of reach of current and upcoming facilities, TOI-700 d provides a rare opportunity to measure the planet’s mass with state-of-the-art facilities like ESPRESSO on the VLT (Pepe et al. 2010). Future observations should focus on measuring the mass of all three planets to gain insight into whether or not Earth-sized planets around low-mass stars are similar to Earth. The TESS mission was recently selected for its first extended mission, which will begin in the summer of 2020. According to the draft observing schedule, TOI-700 will be observed in 11 more sectors during TESS cycle 3,³⁵ providing a great opportunity to refine the ephemerides and parameters of the three known planets and possibly detect additional planets in the system that would enhance our understanding of TOI-700’s architecture.

A.V.’s work was performed under contract with the California Institute of Technology (Caltech)/Jet Propulsion Laboratory (JPL) funded by NASA through the Sagan Fellowship Program executed by the NASA Exoplanet Science Institute. M.N.G. acknowledges support from MIT’s Kavli Institute as a Juan Carlos Torres Fellow. C.D.D. acknowledges support from the NASA TESS Guest Investigator Program through grant 80NSSC18K1583. E.D.L. is thankful for support from GSFC Sellers Exoplanet Environments Collaboration (SEEC), which is funded by the NASA Planetary Science Divisions Internal Scientist Funding Model. J.N.W. thanks the Heising-Simons Foundation for support. E.A.G. thanks the LSSTC Data Science Fellowship Program, which is funded by LSSTC, NSF Cybertraining grant #1829740, the Brinson Foundation, and the Moore Foundation; her participation in the program has benefited this work. E.A.G. is thankful for support from GSFC Sellers Exoplanet Environments Collaboration (SEEC), which is funded by the NASA Planetary Science Division’s Internal Scientist Funding Model.

This work is based on observations made with the Spitzer Space Telescope, which is operated by the Jet Propulsion Laboratory, California Institute of Technology under a contract with NASA. Support for this work was provided by NASA through an award issued by JPL/Caltech. This research has made use of SAO/NASA’s Astrophysics Data System Bibliographic Services. This research has made use of the SIMBAD database, operated at CDS, Strasbourg, France. This work has made use of data from the European Space Agency (ESA) mission Gaia (<https://www.cosmos.esa.int/gaia>), processed by the Gaia Data Processing and Analysis Consortium (DPAC; <https://www.cosmos.esa.int/web/gaia/dpac/consortium>). Funding for the DPAC has been provided by national institutions, in particular the institutions participating in the Gaia Multilateral Agreement. This work makes use of observations from the Las Cumbres Observatory Global Telescope Network. We thank Kevin Stevenson for making the POET pipeline open source and freely available on GitHub.

Funding for the TESS mission is provided by NASA’s Science Mission directorate. We acknowledge the use of public TESS Alert data from pipelines at the TESS Science Office and



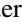
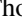
³⁵ <https://heasarc.gsfc.nasa.gov/cgi-bin/tess/webtess/wtv.py>












at the TESS Science Processing Operations Center. This research has made use of the NASA Exoplanet Archive and the Exoplanet Follow-up Observation Program website, which are operated by the California Institute of Technology, under contract with the National Aeronautics and Space Administration under the Exoplanet Exploration Program. This paper includes data collected by the TESS mission, which are publicly available from the Mikulski Archive for Space Telescopes (MAST). This paper includes observations obtained under Gemini program GN-2018B-LP-101. Resources supporting this work were provided by the NASA High-End Computing (HEC) Program through the NASA Advanced Supercomputing (NAS) Division at Ames Research Center for the production of the SPOC data products.

Facilities: TESS, Spitzer, LCOGT, Gaia, MAST.

Software: EXOFASTv2 (Eastman et al. 2013, 2019), AstroImageJ (Collins et al. 2017), BATMAN (Kreidberg 2015), Forecaster (Chen & Kipping 2017).

ORCID iDs

Joseph E. Rodríguez  <https://orcid.org/0000-0001-8812-0565>
 Andrew Vanderburg  <https://orcid.org/0000-0001-7246-5438>
 Sebastian Zieba  <https://orcid.org/0000-0003-0562-6750>
 Laura Kreidberg  <https://orcid.org/0000-0003-0514-1147>
 Caroline V. Morley  <https://orcid.org/0000-0002-4404-0456>
 Jason D. Eastman  <https://orcid.org/0000-0003-3773-5142>
 Stephen R. Kane  <https://orcid.org/0000-0002-7084-0529>
 Samuel N. Quinn  <https://orcid.org/0000-0002-8964-8377>
 Ryan Cloutier  <https://orcid.org/0000-0001-5383-9393>
 Chelsea X. Huang  <https://orcid.org/0000-0003-0918-7484>
 Karen A. Collins  <https://orcid.org/0000-0001-6588-9574>
 Andrew W. Mann  <https://orcid.org/0000-0003-3654-1602>
 Emily Gilbert  <https://orcid.org/0000-0002-0388-8004>
 Joshua E. Schlieder  <https://orcid.org/0000-0001-5347-7062>
 Elisa V. Quintana  <https://orcid.org/0000-0003-1309-2904>
 Thomas Barclay  <https://orcid.org/0000-0001-7139-2724>
 Gabrielle Suissa  <https://orcid.org/0000-0003-4471-1042>
 Ravi kumar Kopparapu  <https://orcid.org/0000-0002-5893-2471>
 Courtney D. Dressing  <https://orcid.org/0000-0001-8189-0233>
 George R. Ricker  <https://orcid.org/0000-0003-2058-6662>
 Roland K. Vanderspek  <https://orcid.org/0000-0001-6763-6562>
 David W. Latham  <https://orcid.org/0000-0001-9911-7388>
 Sara Seager  <https://orcid.org/0000-0002-6892-6948>
 Joshua N. Winn  <https://orcid.org/0000-0002-4265-047X>
 Jon M. Jenkins  <https://orcid.org/0000-0002-4715-9460>
 Zachory Berta-Thompson  <https://orcid.org/0000-0002-3321-4924>
 Patricia T. Boyd  <https://orcid.org/0000-0003-0442-4284>
 David Charbonneau  <https://orcid.org/0000-0002-9003-484X>
 Douglas A. Caldwell  <https://orcid.org/0000-0003-1963-9616>
 Eugene Chiang  <https://orcid.org/0000-0002-6246-2310>
 Jessie L. Christiansen  <https://orcid.org/0000-0002-8035-4778>
 David R. Ciardi  <https://orcid.org/0000-0002-5741-3047>
 Knicole D. Colón  <https://orcid.org/0000-0001-8020-7121>

John Doty  <https://orcid.org/0000-0003-2996-8421>
 Tianjun Gan  <https://orcid.org/0000-0002-4503-9705>
 Natalia Guerrero  <https://orcid.org/0000-0002-5169-9427>
 Maximilian N. Günther  <https://orcid.org/0000-0002-3164-9086>
 Eve J. Lee  <https://orcid.org/0000-0002-1228-9820>
 Alan M. Levine  <https://orcid.org/0000-0001-8172-0453>
 Eric Lopez  <https://orcid.org/0000-0002-7727-4603>
 Philip S. Muirhead  <https://orcid.org/0000-0002-0638-8822>
 Elisabeth Newton  <https://orcid.org/0000-0003-4150-841X>
 Mark E. Rose  <https://orcid.org/0000-0003-4724-745X>
 Joseph D. Twicken  <https://orcid.org/0000-0002-6778-7552>

References

- Akeson, R. L., Chen, X., Ciardi, D., et al. 2013, *PASP*, 125, 989
 Barnes, R. 2017, *CeMDA*, 129, 509
 Batalha, N. E., Kempton, E. M.-R., & Mbarek, R. 2017, *ApJL*, 836, L5
 Beichman, C., Benneke, B., Knutson, H., et al. 2014, *PASP*, 126, 1134
 Borucki, W. J., Agol, E., Fressin, F., et al. 2013, *Sci*, 340, 587
 Borucki, W. J., Koch, D., Basri, G., et al. 2010, *Sci*, 327, 977
 Brown, T. M., Baliber, N., Bianco, F. B., et al. 2013, *PASP*, 125, 1031
 Burke, C. J., Mullally, F., Thompson, S. E., Coughlin, J. L., & Rowe, J. F. 2019, *AJ*, 157, 143
 Charbonneau, D., Allen, L. E., Megeath, S. T., et al. 2005, *ApJ*, 626, 523
 Chen, J., & Kipping, D. 2017, *ApJ*, 834, 17
 Choi, J., Dotter, A., Conroy, C., et al. 2016, *ApJ*, 823, 102
 Claret, A. 2017, *A&A*, 600, A30
 Cloutier, R., & Menou, K. 2020, *AJ*, 159, 211
 Collins, K. A., Kielkopf, J. F., Stassun, K. G., & Hessman, F. V. 2017, *AJ*, 153, 77
 Cubillos, P., Harrington, J., Madhusudhan, N., et al. 2013, *ApJ*, 768, 42
 Cutri, R. M., Skrutskie, M. F., van Dyk, S., et al. 2003, *yCat*, 2246, 0
 Cutri, R. M., et al. 2014, *yCat*, 2328, 0
 Désert, J.-M., Charbonneau, D., Torres, G., et al. 2015, *ApJ*, 804, 59
 Dittmann, J. A., Irwin, J. M., Charbonneau, D., et al. 2017, *Natur*, 544, 333
 Dressing, C. D., & Charbonneau, D. 2015, *ApJ*, 807, 45
 Dressing, C. D., Charbonneau, D., Dumusque, X., et al. 2015, *ApJ*, 800, 135
 Eastman, J., Gaudi, B. S., & Agol, E. 2013, *PASP*, 125, 83
 Eastman, J. D., Rodríguez, J. E., Agol, E., et al. 2019, arXiv:1907.09480
 Faria, J. P., Adibekyan, V., Amazo-Gómez, E. M., et al. 2020, *A&A*, 635, A13
 Fazio, G. G., Hora, J. L., Allen, L. E., et al. 2004, *ApJS*, 154, 10
 Foreman-Mackey, D., & Barentsen, G. 2019, *dfm/exoplanet: exoplanet v0.1.3*, Zenodo, doi:10.5281/zenodo.2536576
 Fulton, B. J., Petigura, E. A., Howard, A. W., et al. 2017, *AJ*, 154, 109
 Gaia Collaboration, Brown, A. G. A., Vallenari, A., et al. 2018, *A&A*, 616, A1
 Gardner, J. P., Mather, J. C., Clampin, M., et al. 2006, *SSRv*, 123, 485
 Gaudi, B. S., Seager, S., Mennesson, B., et al. 2018, *NatAs*, 2, 600
 Gilbert, E. A., Barclay, T., Schlieder, J. E., et al. 2020, *AJ*, 160, 116
 Gillon, M., Triaud, A. H. M. J., Demory, B.-O., et al. 2017, *Natur*, 542, 456
 Goodman, J., & Weare, J. 2010, *CAMCS*, 5, 65
 Günther, M. N., Pozuelos, F. J., Dittmann, J. A., et al. 2019, *NatAs*, 3, 1099
 Jenkins, J. M. 2002, *ApJ*, 575, 493
 Jenkins, J. M., Twicken, J. D., McCauliff, S., et al. 2016, *Proc. SPIE*, 9913, 99133E
 Jensen, E. 2013, Tapir: A web interface for transit/eclipse observability, Astrophysics Source Code Library, ascl:1306.007
 Kaltenegger, L., Pepper, J., Stassun, K., & Oelkers, R. 2019, *ApJL*, 874, L8
 Kane, S. R. 2014, *ApJ*, 782, 111
 Kane, S. R. 2018, *ApJL*, 861, L21
 Kane, S. R., & Gelino, D. M. 2012, *PASP*, 124, 323
 Kane, S. R., Hill, M. L., Kasting, J. F., et al. 2016, *ApJ*, 830, 1
 Kasting, J. F., Whitmire, D. P., & Reynolds, R. T. 1993, *Icar*, 101, 108
 Kipping, D. M. 2013, *MNRAS*, 435, 2152
 Kopparapu, R. K., Ramirez, R., Kasting, J. F., et al. 2013, *ApJ*, 765, 131
 Kopparapu, R. K., Ramirez, R. M., SchottelKotte, J., et al. 2014, *ApJL*, 787, L29
 Kreidberg, L. 2015, *PASP*, 127, 1161
 Kreidberg, L., Bean, J. L., Désert, J.-M., et al. 2014, *Natur*, 505, 69
 Kreidberg, L., Koll, D. D. B., Morley, C., et al. 2019, *Natur*, 573, 87
 Li, J., Tenenbaum, P., Twicken, J. D., et al. 2019, *PASP*, 131, 024506
 Liddle, A. R. 2007, *MNRAS*, 377, L74
 Line, M. R., Stevenson, K. B., Bean, J., et al. 2016, *AJ*, 152, 203

- Mandel, K., & Agol, E. 2002, *ApJL*, **580**, L171
- Mann, A. W., Dupuy, T., Kraus, A. L., et al. 2019, *ApJ*, **871**, 63
- Mann, A. W., Feiden, G. A., Gaidos, E., Boyajian, T., & von Braun, K. 2015, *ApJ*, **804**, 64
- Ment, K., Dittmann, J. A., Astudillo-Defru, N., et al. 2019, *AJ*, **157**, 32
- Morley, C. V., Kreidberg, L., Rustamkulov, Z., Robinson, T., & Fortney, J. J. 2017, *ApJ*, **850**, 121
- Morton, T. D., Bryson, S. T., Coughlin, J. L., et al. 2016, *ApJ*, **822**, 86
- Mullally, F., Thompson, S. E., Coughlin, J. L., Burke, C. J., & Rowe, J. F. 2018, *AJ*, **155**, 210
- Pepe, F., Molaro, P., Cristiani, S., et al. 2014, arXiv:1401.5918
- Pepe, F. A., Cristiani, S., Rebolo Lopez, R., et al. 2010, *Proc. SPIE*, **7735**, 77350F
- Pont, F., Zucker, S., & Queloz, D. 2006, *MNRAS*, **373**, 231
- Quintana, E. V., Barclay, T., Raymond, S. N., et al. 2014, *Sci*, **344**, 277
- Ricker, G. R., Winn, J. N., Vanderspek, R., et al. 2015, *JATIS*, **1**, 014003
- Roberge, A., & Moustakas, L. A. 2018, *NatAs*, **2**, 605
- Rogers, L. A. 2015, *ApJ*, **801**, 41
- Schwarz, G. 1978, *AnSta*, **6**, 461
- Smith, J. C., Stumpe, M. C., van Cleve, J. E., et al. 2012, *PASP*, **124**, 1000
- Stassun, K. G., & Torres, G. 2018, *ApJ*, **862**, 61
- Stevenson, K. B., Harrington, J., Fortney, J. J., et al. 2012, *ApJ*, **754**, 136
- Stumpe, M. C., Smith, J. C., Catanzarite, J. H., et al. 2014, *PASP*, **126**, 100
- Suissa, G., Wolf, E. T., Kopparapu, R. k., et al. 2020, *AJ*, **160**, 118
- Sullivan, P. W., Winn, J. N., Berta-Thompson, Z. K., et al. 2015, *ApJ*, **809**, 77
- Szentgyorgyi, A., Baldwin, D., Barnes, S., et al. 2016, *Proc. SPIE*, **9908**, 990822
- Torres, G., Kipping, D. M., Fressin, F., et al. 2015, *ApJ*, **800**, 99
- Twicken, J. D., Catanzarite, J. H., Clarke, B. D., et al. 2018, *PASP*, **130**, 064502
- Vanderburg, A., & Johnson, J. A. 2014, *PASP*, **126**, 948
- Vanderburg, A., Rowden, P., Bryson, S., et al. 2020, *ApJL*, **893**, L27
- Vanderspek, R., Huang, C. X., Vanderburg, A., et al. 2019, *ApJL*, **871**, L24
- Weiss, L. M., & Marcy, G. W. 2014, *ApJL*, **783**, L6
- Winn, J. N., Holman, M. J., Bakos, G. Á, et al. 2007, *AJ*, **134**, 1707
- Winn, J. N., Holman, M. J., Torres, G., et al. 2008, *ApJ*, **683**, 1076
- Winters, J. G., Medina, A. A., Irwin, J. M., et al. 2019, *AJ*, **158**, 152
- Wolfgang, A., & Lopez, E. 2015, *ApJ*, **806**, 183
- Yang, J., Abbot, D. S., Koll, D. D. B., Hu, Y., & Showman, A. P. 2019, *ApJ*, **871**, 29
- Yang, J., Cowan, N. B., & Abbot, D. S. 2013, *ApJL*, **771**, L45
- Zeng, L., Sasselov, D. D., & Jacobsen, S. B. 2016, *ApJ*, **819**, 127